ARTICLE   OPEN

Domain wall-localized phonons in BiFeO₃: spectrum and selection rules

Peng Chen[1 ✉], Louis Ponet[1,2], Keji Lai[3], Roberto Cingolani[1] and Sergey Artyukhin[1 ✉]

Ferroelectric domain walls (DWs) are nanoscale topological defects that can be easily tailored to create nanoscale devices. Their excitations, recently discovered to be responsible for GHz DW conductivity, hold promise for faster signal transmission and processing compared to the existing technology. Here we find that DW phonons have unprecedented dispersion going from GHz all the way to THz frequencies, and resulting in a surprisingly broad GHz signature in DW conductivity. Puzzling activation of nominally forbidden DW sliding modes in BiFeO₃ is traced back to DW tilting and resulting asymmetry in wall-localized phonons. The obtained phonon spectra and selection rules are used to simulate scanning impedance microscopy, emerging as a powerful probe in nanophononics. The results will guide the experimental discovery of the predicted phonon branches and design of DW-based nanodevices operating in the technologically important frequency range.

INTRODUCTION

The seminal work of Seidel et al.[1] demonstrated that DC conductivity is higher at domain walls (DWs) in BiFeO₃ (BFO) than in the bulk, enabling signal transmission along the walls. This inspired a new paradigm for the design of DW-based nanoelectronic devices[2,3,4–12], leading to the demonstration of DW-based diode and transistor operating in kHz range[6,12]. The push for higher frequencies[13–15], used in modern computers, has led to a discovery of giant increase of the effective DW conductivity at GHz frequencies in recent microwave microscopy experiments[15,16,17]. The conductivity results from the excitation of soft DW-localized phonon modes, that are at the heart of switching, microwave dielectric loss, and dielectric constant enhancement in ferroelectrics[15,18,19]. They correspond to oscillations of the DW plane and can be excited by an AC electric field that favors one of the domains during its half period (Fig. 1a). Here we show that the frequency of these phonons can go from GHz all the way up to THz, going beyond the frequency range of modern surface acoustic wave-based cell phone transducers.

The results explain why the frequency range of the scanning microwave impedance microscopy (SMIM) anomaly is so wide and reveal DW-localized bands in the phonon spectra of ferroelectrics. We also address the peculiar selection rules for DW excitation. When the ferroelectric polarization component along the driving field is the same in the two domains across the wall, the DW vibration should not be excited (Fig. 1b), as seen at 180° walls on the *ac* face of YMnO₃[15]. However, this rule is violated in recent experiments on rhombohedral BFO, where polarization components along the field across the wall do not differ (Fig. 1c), while the DW mode is still excited and the effect is robust against extrinsic artefacts such as oxygen and bismuth vacancies, tip–sample interface, and Schottky barriers[18]. The results could inspire the exploration of DW-based nanosystems in THz frequency range, and lead to novel DW-based phononic nanodevices.

BFO is a rare room-temperature multiferroic with the largest spontaneous polarization among single-phase compounds known

to date, and may be soon used in nano-devices[20]. Three types of ferroelectric DWs in the rhombohedral phase are distinguished by the number of polarization components being reversed[21]. The most puzzling data is on R71° DWs, at which the P_2 component is reversed, and the polarization rotates by 71° across the wall, as seen in Fig. 1c. R71 DWs are often seen in BFO films grown on a [001] oriented substrate[22,23], such as SrTiO₃ and DyScO₃. The sliding mode of this wall should not be excited by the field normal to the (100) surface, since neither domain is favored by the field, as seen in Fig. 1c. However, the AC impedance signal is still observed experimentally[18], and exceeds DC conductivity by 5–6 orders of magnitude, thus significantly exceeding the possible contribution due to charged defects[24,25]. The important distinction between 180° DWs in YMnO₃ and R71 DWs in BFO is their orientation with respect to the surface. YMnO₃ DWs are mostly normal to the surface, while BFO R71 DWs are tilted away from the surface normal. In that case the combination of the surface and DW orientations breaks the symmetry, as seen in Fig. 1c. This symmetry breaking plays a key role in their response to electric fields, even when the simple selection rule, summarized in Fig. 1a, b, suggests no response.

RESULTS

DW-localized phonons

We use the Ginzburg–Landau–Devonshire (GLD) model for DWs in BFO to capture the energetics of interacting ferroelectric polarization and strain (see Methods for details). The DW is tilted 45° away from the surface normal and bends near the surface to reduce the DW area, as shown in Fig. 2. Long-range strain textures emanate from the bent segments. P_3 decrease in the blue area near the surface is driven by the compression ϵ_{33} and the tensile strain ϵ_{11} via electrostriction.

The vibrational modes of the system with DWs are computed from the linearized equations of motion within a discretized Ginzburg–Landau model, and shown in Fig. 3a, b (see the Methods section for details). The DW breaks translational

---

¹Quantum Materials Theory, Istituto Italiano di Tecnologia, 16163 Genova, Italy. ²Scuola Normale Superiore di Pisa, 56126 Pisa, Italy. ³Department of Physics, University of Texas at Austin, Austin, TX 78712, USA. ✉email: pc011@uark.edu; Sergey.Artyukhin@iit.it
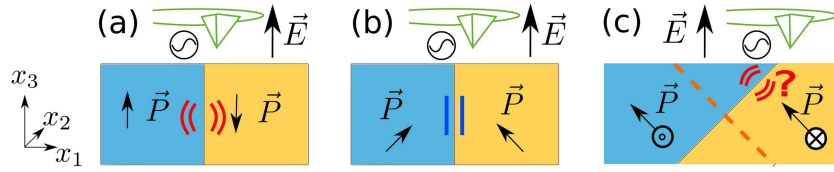
Fig. 1 Selection rules for activation of DW sliding modes under the electric field applied by the SMIM tip. a Excitation of a DW sliding mode is allowed when the field favors one of the domains; **b, c** when the field from the tip has the same projection on the polarizations of two domains, the excitation of the DW sliding mode is forbidden. **c** 71° domain wall corresponding to the P_2 reversal in BFO. The wall is tilted to minimize the elastic energy due to strain mismatch between the two domains, thus breaking the mirror indicated with a dashed line. The pseudocubic coordinates x_1, x_2, x_3 shown here are used throughout the paper and are referred to as the horizontal, out-of-plane and vertical directions.
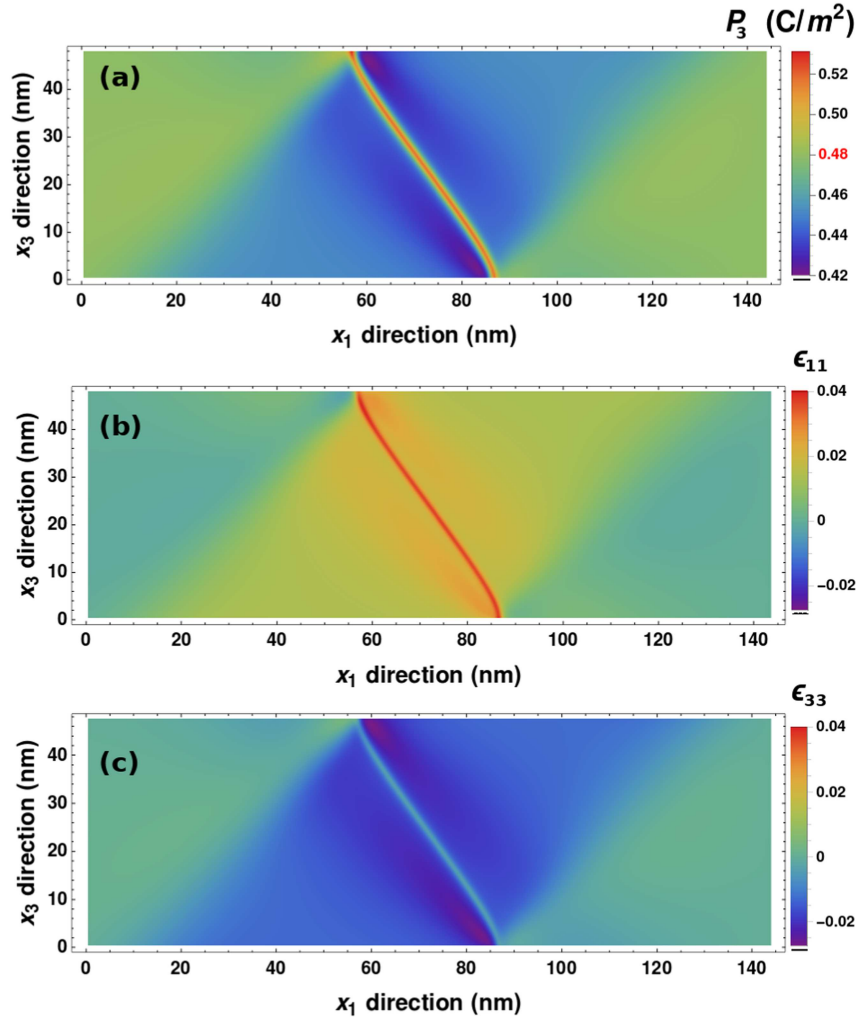

Fig. 2 Electric polarization and strain profiles at an R71 DW. Asymmetric polarization (**a**) and strain profiles (**b, c**) at the domain wall obtained by numerical energy minimization. Each polarization component in the bulk takes the value, marked in red on the color scale in **a**.

invariance and therefore the modes are not characterized by a well-defined quasimomentum. The traditional phonon band structure is then replaced by a spectral function, as seen in Fig. 3a, where the intensity at frequency ω and wavevector k indicates the content of plane waves with that wavevector in the eigenmodes at that frequency. For a translationally invariant system, sharp peaks would then appear in the spectral function

$$A_j\left(\omega, \vec{k}\right) = \sum_\nu \delta(\omega \pm \omega_\nu) \left| \left\langle \delta P_{j,\nu}(r) \left| \exp\left(i\vec{k} \cdot \vec{r}\right) \right\rangle \right. \right|^2$$ at frequencies

ω_ν of phonon modes ν, where $\delta P_{j,\nu}(r)$ is the polarization profile due to the mode ν of unit amplitude. The long-ranged strain texture of the wall, shown in Fig. 2, is responsible for strong

mixing between the DW sliding modes and acoustic phonons, whose frequency ranges overlap. This mixing is evident from the rays in the phonon polarization profile δP_3, Fig. 3c (lower), repeating the shape of the strain texture, Fig. 2.

Figure 3a, b shows for every frequency ω the content of plane waves with $P_2 \sim e^{i\vec{k} \cdot \vec{r}}$ in modes of that frequency, while Fig. 3d shows the phonon dispersion along the wall. At low frequencies acoustic phonons are observed (their intensity is divided by 10 in Fig. 3d to make the DW branch visible). They correspond to strain modulations and mix with P_2 modes due to electrostriction, $f_q = -\frac{1}{2}\epsilon_{jk}q_{jklm}P_lP_m$. The V-shaped low frequency branch, marked with (1–3) in Fig. 3a, extends from around 10 GHz at Γ-point all the
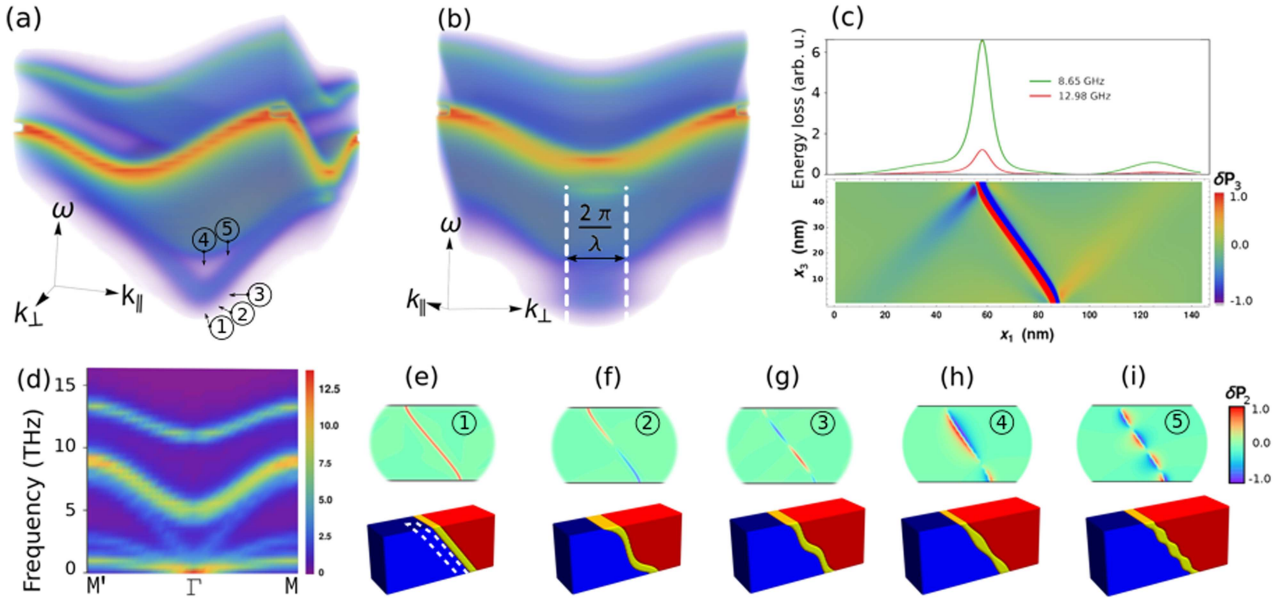
Fig. 3 DW-localized phonons and their SMIM signatures. a, b The phonon spectral function for polar modes in BFO with an R71 DW. The intense bands are the polar modes. The faint stripe at low energy, merging with the phonon band away from the zone center corresponds to the DW sliding modes. The labels in **a**, ①~⑤, are used to indicate the DW localized modes in **e–i** with correspondingly the same labels. The spectral weight extends to $k \sim 2\pi/\lambda$ in the direction perpendicular to the wall, as seen in panel **b. c** The simulated SMIM loss signal across R71 DW $I(r, \omega)$. A peak at the DW and a signature from the long-range strain profile are seen at the sliding mode frequency. The notable asymmetry in the polarization profile, $\delta P_3(r)$ for the DW sliding mode that leads to the excitation of this mode by the vertical electric field is shown below; **d** the spectral function for both polar and acoustic phonons along the $k_\parallel$ direction (a cross-section of (**a**) and (**b**) through the Γ point). **e–i** Real-space polarization profile $\delta P_2(r)$ of the low frequency DW sliding **e–g** and breathing **h, i** modes (upper row), along with schematic illustrations of corresponding DW vibrations (below). The initial position of the DW is marked with white dashed lines.

way to the bulk polar phonons, and corresponds to the DW sliding and wobbling modes, illustrated in Fig. 3e–g. The phonons in this branch disperse along the wall (along $k_\parallel$), but are localized in the perpendicular direction, and therefore their Fourier components extend to $k_\perp \sim \pm\pi/\lambda$, where λ stands for the DW width. The intensity of the DW-localized branch is lower than that of the bulk phonons due to the low volume fraction occupied by DWs. The higher frequency modes are the bulk polar phonons.

Figure 3e–i shows δP_2 profiles corresponding to some of the lowest frequency DW sliding modes (e–g) and breathing modes (h, i). The nodeless mode shown in the upper panel of Fig. 3e corresponds to the P_2 increase at the wall during half-period of the oscillation, therefore adding the DW area to the positive domain. During another half-period the negative domain grows. Therefore this mode can be thought of as DW sliding, depicted schematically in the lower panels of Fig. 3e. A higher energy mode with a node in that branch, shown in the upper panel of Fig. 3f, corresponds to DW wobbling. The DW breathing modes, schematically shown in Fig. 3h, i, are found below the band of bulk polar modes, and are indicated with markers (4 and 5) in Fig. 3a.

SMIM signal simulations

Now we move to the origin of the SMIM signal. In the experiments, an AC electric field is applied between the tip and the back electrode, as shown in Fig. 1, and the current is measured. The phonons that have a non-zero energy in the oscillating field of the tip, $-\int dr \delta \vec{P}(\vec{r}) \cdot \vec{E}(\vec{r}) e^{i\omega t}$, are excited and give rise to a displacement current component in phase with the field. The corresponding loss, $\text{Re} \int dr \vec{j}(r) \cdot \vec{E}(r)$ is measured in addition to the Ohmic losses due to itinerant electrons. The amplitude x_j of a phonon mode j with an eigenfrequency ω_j is governed by the equation of motion

$$m_j\ddot{x}_j + \gamma_j\dot{x}_j + m_j\omega_j^2 x_j = \int dr \delta \vec{P}_j(\vec{r}) \cdot \vec{E}(\vec{r}) e^{i\omega t}, \quad (1)$$

where the mode is characterized by its effective mass m_j, damping γ_j, and the spatial polarization profile $\delta P_j(r)$. The oscillating driving force on the right-hand side is due to the electric field $\vec{E}(\vec{r}) e^{i\omega t}$ of the SMIM tip. The tip function $E(r)$ mimics the electrostatic potential arising due to a voltage applied between the tip and the back electrode. It is a sum of the potential of a point charge, placed 20 nm above the surface, and an opposite image charge due to the back electrode. Damping of $\gamma = 0.1$ THz was used throughout the manuscript for illustration purposes, as we leave phonon–phonon interactions and phonon damping outside the scope of the present study. Looking for the solution in the form $x_j = x_j^{(0)} e^{i\omega t}$, we obtain the loss power at the tip position $\vec{r}$,

$$I(\vec{r}, \omega) = \omega^2 \gamma \sum_j \frac{\left[\int dr' \vec{E}\left(\vec{r}' - \vec{r} \right) \cdot \delta \vec{P}_j\left(\vec{r}' \right) \right]^2}{m_j^2 \left(\omega_j^2 - \omega^2 \right)^2 + \omega^2 \gamma^2}. \quad (2)$$

The frequency dependence is characterized by a Lorentzian. The integral in the numerator is negligible for phonons whose spatial oscillation period is much smaller than the length scale of the electric field inhomogeneity, roughly determined by the tip radius R, therefore the phonons with wavevectors $k \lesssim R^{-1}$ are excited. Figure 3c shows the simulated signal for a BFO sample containing a R71 DW. An asymmetric peak at the DW and a weak signature due to the long-range strain features are visible. We note that Eq. (2) only describes the phonon contributions to SMIM signal, i.e., the contribution of bound charges. It does not capture contributions of itinerant carriers, mobile defects[24], and artefacts seen in SMIM due to surface topography and Schottky barriers[26].

DISCUSSION

Figure 3c shows that SMIM conductivity is much higher at DW than in the bulk due to low-frequency DW sliding and wobbling modes. Their dispersion spans the whole GHz range and extends
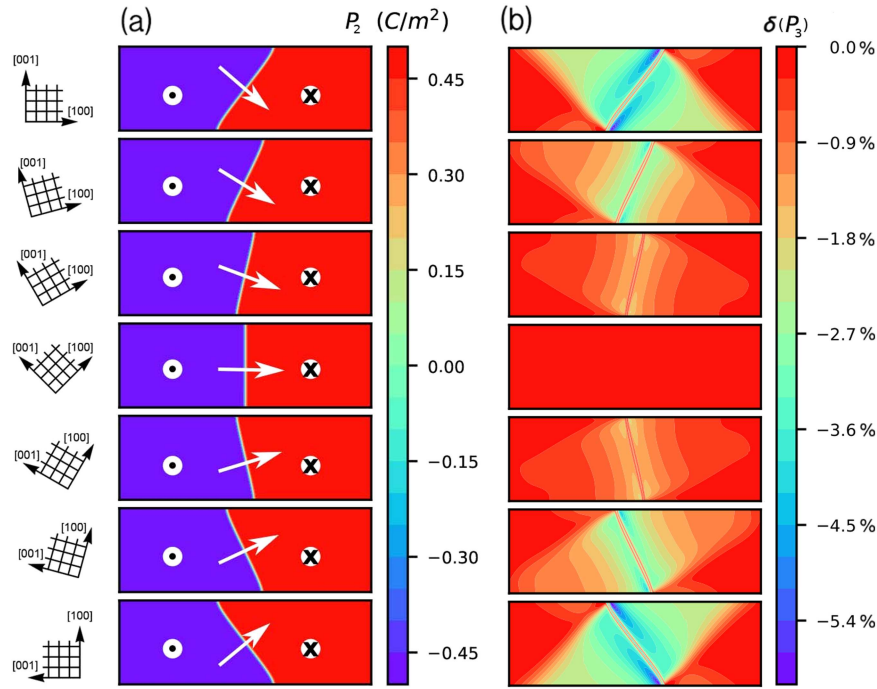
Fig. 4 Asymmetric ferroelectric polarization at an R71 DW. a Thin films with various surface orientations with respect to the crystallographic directions, indicated on the left. The DW normal is indicated by the arrow. **b** Normalized deviation of the vertical component of polarization $\delta(P_3) = \frac{P_3(r) - P_{3,bulk}}{P_{3,bulk}}$ from its bulk value $P_{3,bulk}$ due to the stress at the DW.

to the bulk polar phonon band, usually positioned at THz frequency. This explains why the GHz microwave conductivity at DWs in hexagonal manganites does not show a narrow peak in the frequency domain, but rather rises monotonically towards higher frequencies. The proximity of DW phonons to acoustic branches also leads to phonon scattering and affects thermal conductivity[27]. The low frequency of sliding modes is also behind the giant enhancement of the static dielectric permittivity[19]. In addition, soft DW phonons are responsible for mechanical softening phenomena, recently observed in several ferroelectrics[28].

In materials with strong strain–polarization interactions, DWs are aligned into regular lattices by strain fields[29,30], and spectral features similar to the ones in Fig. 3a, b are expected. Alternatively, when DWs are randomly oriented, the spectral weight of DW wobbling and breathing modes spreads along different directions, but the phonon density of states is expected to retain its shape, with the peak at GHz frequencies. The directionality of DWs and their populations in the sample can then be inferred from the orientation and intensity of low-energy branches, as discussed in Supplementary Note 2 and Supplementary Fig. 2.

The recent observation of nominally silent DW modes in BFO[18] being activated is a surprising evidence that DW type and orientation control local AC conductivity. Possible DW orientations have been classified using symmetry and compatibility analyses[31,32]. In essence, the distances between ionic planes in the two domains must match along the wall. This is only possible for particular DW orientations, for which the strain components in the DW plane match at the wall (see Supplementary Eq. (3)). The energy penalty (see Supplementary Note 1 and Supplementary Fig. 1) for violating this condition scales linearly with the wall area, therefore fixing the DW orientation in the bulk. However, in thin films surface strain relaxation allows the DW to deviate from its optimal bulk orientation.

In an infinite bulk sample with a DW, a diagonal mirror plane $M_{dw}(-1, 0, 1)$, shown by the dashed line in Fig. 1c, is a symmetry operation. This symmetry imposes the requirements: $\epsilon_{11} = \epsilon_{33}$, ϵ_{12}

$= \epsilon_{23}$. The surface of the thin film and the domain wall orientation together break this mirror symmetry m_{dw} if they are not orthogonal. The stress at the tilted domain wall $\sigma_{jk} = \partial f/\partial \epsilon_{jk}$ then acts on geometrically different regions from the left and right sides of the wall. The resulting asymmetric strain induces asymmetric polarization across the wall via electrostriction, Eq. (7). This phenomenon is observed in Fig. 4, where we simulated thin films with different surface orientations with respect to the crystallographic directions (different ways of cutting a film out of a slab). It is seen that the DW orients perpendicular to the $[P_1, 0, P_3]$ direction, and a small bending near the surface is observed in Fig. 4a[33–36]. In very thin films, the wall deviates from the [101] orientation towards the surface normal. Figure 4b shows the polarization component normal to the surface. When the wall is tilted at 45°, the asymmetry of the polarization P_3 is evident in Fig. 2a, especially near the surface where the polarization deviates the most from the bulk value. This asymmetry comes from the asymmetric strain, plotted in Fig. 2b, c. Even though the DW polarization profile is very narrow, the accompanying strain texture, emanating from the areas of DW bending near the surface[33–36], extends surprisingly far[37,38], as seen in Fig. 2b, c.

The polarization asymmetry eventually results in the asymmetry in the phonon polarization profile of the DW sliding mode, as seen in the lower panel of Fig. 3c. When the polarization component P_3 interacts with the external electric field, normal to the surface, the electrostatic energy $-\int dr \vec{E}(\vec{r}) \cdot \vec{P}(\vec{r} - \vec{r}_{DW})$ results in a force on the wall due to $\vec{E} \cdot \frac{\partial \vec{P}(\vec{r} - \vec{r}_{DW})}{\partial x_{1,DW}} \neq 0$ and excitation of the DW vibration by the SMIM field.

In addition to SMIM, it may be possible to observe the DW-localized modes with inelastic neutron or X-ray scattering, although their intensity may be low due to low volume fraction occupied by DWs. Rapid quenching of a sample across the ferroelectric transition, leading to high DW densities[39], or strain-induced generation and alignment of ferroelastic DWs[40] should increase the intensity of these branches and enable their

observation in inelastic neutron scattering experiments and other bulk spectroscopies.

In summary, the simulated phonon spectra reveal the DW-localized phonon branches starting from GHz and extending all the way to THz frequencies. This explains a wide frequency range of the conductivity anomaly observed in hexagonal manganites[15] and other materials. The surprising activation of the nominally silent DW mode at R71° DWs in BFO is interpreted in terms of phonon polarization asymmetry due to the interplay of electrostriction and elastic compatibility at a tilted DW. The proposed way to simulate SMIM experiments may be used in emerging second-principles methodologies. Since the low-energy theory used here is rather general, similar phonon spectra must be expected for all ferroic materials, where the order parameter couples strongly to the lattice. We hope this work will motivate the experimental search for DW-localized phonon branches, guide the interpretation of SMIM studies and eventually inspire the development of high-speed DW-based phononic devices, extending surface acoustic wave-based technology to THz DW-based circuits.

METHODS

Computational

In order to elucidate the essential physics that is responsible for the activation of the tilted R71 walls, we use a simplified GLD model[41]. To this end, we focus on the polar mode that connects the parent centrosymmetric phase with the ferroelectric one and consider its interactions with strains (through electrostriction), while neglecting octahedral rotations.

The free energy density, expanded near the centrosymmetric para-electric parent structure is written as:

$$f = f_L + f_G + f_c + f_q + f_{fl}, \tag{3}$$

$$f_L = a_j P_j^2 + \frac{1}{2} a_{jk} P_j^2 P_k^2 + a_{jkl} P_j^2 P_k^2 P_l^2, \tag{4}$$

$$f_G = \frac{1}{2} G_{jklm} \partial_k P_j \partial_m P_l, \tag{5}$$

$$f_c = \frac{1}{2} \epsilon_{jk} C_{jklm} \epsilon_{lm}, \tag{6}$$

$$f_q = -\frac{1}{2} \epsilon_{jk} q_{jklm} P_l P_m, \tag{7}$$

$$f_{fl} = \frac{1}{2} f_{jklm} (\epsilon_{jk} \partial_m P_l - P_l \partial_m \epsilon_{jk}) \tag{8}$$

where P_j stands for the components of the ferroelectric polarization; the strain tensor ϵ_{jk} is related to symmetrized gradients of deformations u_j as $\epsilon_{jk} = (\partial_k u_j + \partial_j u_k)/2$, where the deformation vector $\vec{u}(\vec{r})$ relates points $\vec{r}$ in the reference structure to $\vec{r} + \vec{u}(\vec{r})$ in the deformed structure; summation over repeated indices is implied. f_L represents the distorted Mexican hat-shaped potential that determines the amplitude and anisotropy of the polarization. f_G describes the energy penalty due to spatial variations of the polarization. f_c describes elastic energy, while f_q is the electrostriction term that refers to the interaction between polarization and strain. The flexoelectric coupling f_{fl} that describes interactions of strain gradient with the polarization, was also included as in ref. [42], but does not change the qualitative results reported here. The parameters of the model were adopted from ref. [43]. To obtain the equilibrium configuration, we minimize the free energy $\int f d^3 r$ in Eq. (3) with respect to $_{Pi}$, u_i, by solving Euler–Lagrange equations with the Lagrangian density given by $-f$, namely $\delta f/\delta_{Pi}(r) = 0$, $\delta f/\delta u_i(r) = 0$ with δ being variational derivatives, using the finite element method as implemented in Fenics software[44,45]. The real space was discretized with element dimensions 0.4 nm. The simulated thin film was 60 nm thick and 180 nm wide, and a single DW was placed in the middle. Test calculations were performed for the 360 nm wide film to validate the long-range strain profile. Zero external stress boundary conditions were applied on the top surface while $u_3 = 0$ was used at the bottom one. At the two ends in the x_1 direction, both open and twisted boundary conditions were tested to ensure the absence of boundary

effects within the domain wall area. Periodic boundary conditions were applied in the translational direction (x_2) to mimic an infinite system.

Phonons are computed using a $20 \times 1 \times 20$ square finite difference mesh with 0.4 nm elements and a single domain wall in the middle. The finite element size gives rise to a periodic lattice potential acting on the DW and gapping the sliding mode at 8 GHz[46]. It is analogous to a Pierls–Nabarro washboard potential in a realistic lattice. The resulting oscillation frequency is an order of magnitude higher than characteristic frequencies of DW vibrations due to electrostatic effects[47].

The energy was minimized numerically and the equations of motion (Euler–Lagrange equations $\delta L/\delta_{Pi}(r) = 0$, $\delta L/\delta u_i(r) = 0$ for the Lagrangian density $L = \frac{1}{2}(M_{uu}\dot{u}^2 + M_{PP}\dot{P}^2) - f(P,u)$) were expanded to a linear order in small deviations $\delta \vec{u}(r,t) = \delta \vec{u}(r)e^{-i\omega t}$, $\delta \vec{P}(r,t) = \delta \vec{P}(r)e^{-i\omega t}$ around the equilibrium state. That leads to a standard generalized eigenvalue problem $F_{jk} v_k^{(n)} = \omega^{(n)} M_{jk} v_k^{(n)}$ for phonon polarization vectors v_k containing all displacement and polarization variations $\delta \vec{u}(r)$, $\delta \vec{P}(r)$; force constants F_{jk} were computed as second derivatives of L and the mass of the polarization mode was chosen to fit the gap between acoustic and optical bands of the spectrum to DFT calculations[48], $M_{PP} \approx 3m_O/V$ and $M_{uu} = (m_{Bi} + m_{Fe} + 3m_O)/V$, where V is the unit cell volume. Phonon polarization vectors were then projected on the plane waves to obtain the phonon spectral functions, shown in Fig. 3a, b, d.

In order to reproduce the realistic 45° tilt of the wall, necessary to simulate the SMIM signal, shown in Fig. 3c, we used a larger grid of $360 \times 1 \times 120$ with 4 nm elements.

DATA AVAILABILITY

The main data supporting the findings of this study are available within the article and its Supplementary Information. Extra data are available from the corresponding author upon reasonable request.

CODE AVAILABILITY

The codes that were used in this study are available at https://github.com/PaulChern/L-INVARIANTS/tree/master/Example.

REFERENCES

1. Seidel, J. et al. Conduction at domain walls in oxide multiferroics. Nat. Mater. **8**, 229–234 (2009).
2. Scott, J. F. Applications of modern ferroelectrics. Science **315**, 954–959 (2007).
3. Tagantsev, A. K., Cross, L. E. & Fousek, J. Domains in Ferroic Crystals and Thin Films (Springer, New York, 2010).
4. Catalan, G., Seidel, J., Ramesh, R. & Scott, J. F. Domain wall nanoelectronics. Rev. Mod. Phys. **84**, 119–156 (2012).
5. Matsubara, M. et al. Multiferroics. Magnetoelectric domain control in multiferroic TbMnO₃. Science **348**, 1112–1115 (2015).
6. McQuaid, R. G. P., Campbell, M. P., Whatmore, R. W., Kumar, A. & Gregg, J. M. Injection and controlled motion of conducting domain walls in improper ferroelectric Cu-Cl boracite. Nat. Commun. **8**, 15105 (2017).
7. Sharma, P. et al. Nonvolatile ferroelectric domain wall memory. Sci. Adv. **3**, e1700512 (2017).
8. Huang, F.-T. & Cheong, S.-W. Aperiodic topological order in the domain configurations of functional materials. Nat. Rev. Mater. **2**, 17004 (2017).
9. Mundy, J. A. et al. Functional electronic inversion layers at ferroelectric domain walls. Nat. Mater. **16**, 622–627 (2017).
10. Turner, P. W. et al. Large carrier mobilities in ErMnO₃ conducting domain walls revealed by quantitative hall-effect measurements. Nano Lett. **18**, 6381–6386 (2018).
11. Akamatsu, H. et al. Light-activated gigahertz ferroelectric domain dynamics. Phys. Rev. Lett. **120**, 096101 (2018).
12. Schaab, J. et al. Electrical half-wave rectification at ferroelectric domain walls. Nat. Nanotechnol. **13**, 1028–1034 (2018).
13. Lee, W. T., Salje, E. K. H. & Bismayer, U. Domain wall diffusion and domain wall softening. J. Phys.: Condens. Matter **15**, 1353–1362 (2003).
14. Scott, J. F., Salje, E. K. H. & Carpenter, M. A. Domain wall damping and elastic softening in SrTiO₃: evidence for polar twin walls. Phys. Rev. Lett. **109**, 187601 (2012).

15. Wu, X. et al. Low-energy structural dynamics of ferroelectric domain walls in hexagonal rare-earth manganites. *Sci. Adv.* **3**, e1602371 (2017).

16. Tselev, A. et al. Microwave a.c. conductivity of domain walls in ferroelectric thin films. *Nat. Commun.* **7**, 11630 (2016).

17. Prosandeev, S., Yang, Y., Paillard, C. & Bellaiche, L. Displacement current in domain walls of bismuth ferrite. *npj Comput. Mater.* **4**, 8 (2018).

18. Huang, Y. L. et al. Unexpected giant microwave conductivity in a nominally silent BiFeO$_3$ domain wall. *Adv. Mater.* **32**, 1905132 (2020).

19. Hlinka, J., Paściak, M., Körbel, S. & Marton, P. Terahertz-range polar modes in domain-engineered BiFeO$_3$. *Phys. Rev. Lett.* **119**, 057604 (2017).

20. Manipatruni, S. et al. Voltage control of unidirectional anisotropy in ferromagnet-multiferroic system. *Sci. Adv.* **4**, eaat4229 (2018).

21. Marton, P., Rychetsky, I. & Hlinka, J. Domain walls of ferroelectric BaTiO$_3$ within the Ginzburg-Landau-Devonshire phenomenological model. *Phys. Rev. B* **81**, 144125 (2010).

22. Ziegler, B., Martens, K., Giamarchi, T. & Paruch, P. Domain wall roughness in stripe phase BiFeO$_3$ thin films. *Phys. Rev. Lett.* **111**, 247604 (2013).

23. Domingo, N., Farokhipoor, S., Santiso, J., Noheda, B. & Catalan, G. Domain wall magnetoresistance in BiFeO$_3$ thin films measured by scanning probe microscopy. *J. Phys.: Condens. Matter* **29**, 334003 (2017).

24. Rojac, T. et al. Domain-wall conduction in ferroelectric BiFeO$_3$ controlled by accumulation of charged defects. *Nat. Mater.* **16**, 322–327 (2017).

25. Liu, L., Rojac, T., Damjanovic, D., Di Michiel, M. & Daniels, J. Frequency-dependent decoupling of domain-wall motion and lattice strain in bismuth ferrite. *Nat. Commun.* **9**, 4928 (2018).

26. Wu, X. et al. Microwave conductivity of ferroelectric domains and domain walls in a hexagonal rare-earth ferrite. *Phys. Rev. B* **98**, 081409 (2018).

27. Royo, M., Escorihuela-Sayalero, C., Íñiguez, J. & Rurali, R. Ferroelectric domain wall phonon polarizer. *Phys. Rev. Mater.* **1**, 051402 (2017).

28. Stefani, C. et al., under review.

29. Artyukhin, S., Delaney, K. T., Spaldin, N. A. & Mostovoy, M. Landau theory of topological defects in multiferroic hexagonal manganites. *Nat. Mater.* **13**, 42–49 (2013).

30. Wang, X. et al. Unfolding of vortices into topological stripes in a multiferroic material. *Phys. Rev. Lett.* **112**, 247601 (2014).

31. Janovec, V. A symmetry approach to domain structures. *Ferroelectrics* **12**, 43–53 (1976).

32. Fousek, J. & Janovec, V. The orientation of domain walls in twinned ferroelectric crystals. *J. Appl Phys.* **40**, 135–142 (1969).

33. Ishibashi, Y. & Salje, E. A theory of ferroelectric 90 degree domain wall. *J. Phys. Soc. Jpn.* **71**, 2800–2803 (2002).

34. Ishibashi, Y., Iwata, M. & Salje, E. Polarization reversals in the presence of 90° domain walls. *Jpn. J. Appl. Phys.* **44**, 7512–7517 (2005).

35. Conti, S. & Weikard, U. Interaction between free boundaries and domain walls in ferroelastics. *Eur. Phys. J. B – Condens. Matter Complex Syst.* **41**, 413–420 (2004).

36. Li, L. et al. Control of domain structures in multiferroic thin films through defect engineering. *Adv. Mater.* **30**, 1802737 (2018).

37. Salje E. K. *Phase Transitions in Ferroelastic and Co-elastic Crystals*. 296 (Cambridge University Press: Cambridge, UK, 1993) 296.

38. Salje, E. K. H., Aktas, O. & Aktas, X. Functional topologies in (multi-) ferroics: the ferroelastic template. In *Topological Structures in Ferroic Materials: Domain Walls, Vortices and Skyrmions* (ed Seidel, J.) 83–101 (Springer International Publishing: Cham, 2016).

39. Griffin, S. M. et al. Scaling behavior and beyond equilibrium in the hexagonal manganites. *Phys. Rev. X* **2**, 041022 (2012).

40. Chae, S. C. et al. Direct observation of the proliferation of ferroelectric loop domains and vortex-antivortex pairs. *Phys. Rev. Lett.* **108**, 167603 (2012).

41. Nambu, S. & Sagala, D. A. Domain formation and elastic long-range interaction in ferroelectric perovskites. *Phys. Rev. B* **50**, 5838–5847 (1994).

42. Park, S. M. et al. Selective control of multiple ferroelectric switching pathways using a trailing flexoelectric field. *Nat. Nanotechnol.* **13**, 366–370 (2018).

43. Saj Mohan, M. M., Bandyopadhyay, S., Jogi, T., Bhattacharya, S. & Ramadurai, R. Realization of rhombohedral, mixed, and tetragonal like phases of BiFeO$_3$ and ferroelectric domain engineering using a strain tuning layer on LaAlO$_3$(001) substrate. *J. Appl. Phys.* **125**, 012501 (2019).

44. Alnæs, M. S. et al. *Archive of Numerical Software* **3** (2015).

45. Logg, A. et al. *Automated Solution of Differential Equations by the Finite Element Method* (Springer, 2012).

46. Marton, P. Discretisation originated Peierls–Nabarro barriers in simulations of ferroelectrics. *Phase Transit.* **91**, 959–968 (2018).

47. Sidorkin, A. S. Domain boundaries in ferroelectrics. *J. Adv. Dielectr.* **02**, 1230013 (2012).

48. Wang, Y. et al. One-pot nonreductive O-glycan release and labeling with 1-phenyl-3-methyl-5-pyrazolone followed by ESI-MS analysis. *Acta Mater.* **59**, 4229–4234 (2011).

AUTHOR CONTRIBUTIONS

P.C. performed the numerical simulations and wrote the initial draft of the manuscript, which was finalized by S.A. and R.C. P.C. and L.P. implemented and carried out the finite-element calculations on the Landau model with input from all authors. K.L. led the experimental efforts that inspired this work. S.A. conceived the project and led the study.

COMPETING INTERESTS

K.L. holds a patent on the MIM technology, which is licensed to PrimeNano, Inc., for commercial instrument. The terms of this arrangement have been reviewed and approved by the University of Texas at Austin in accordance with its policy on objectivity in research. The remaining authors declare no competing interests.

ADDITIONAL INFORMATION

Supplementary information is available for this paper at https://doi.org/10.1038/s41524-020-0304-y.

Correspondence and requests for materials should be addressed to P.C. or S.A.

Reprints and permission information is available at http://www.nature.com/reprints

Publisher's note Springer Nature remains neutral with regard to jurisdictional claims in published maps and institutional affiliations.